Nanoscale

Recent Advances of Novel Ultrathin Two-Dimensional Silicon Carbides from a Theoretical Perspective

Journal:	*Nanoscale*
Manuscript ID	NR-MRV-10-2019-008755.R1
Article Type:	Minireview
Date Submitted by the Author:	17-Dec-2019
Complete List of Authors:	Zhou, Liujiang; University of Electronic Science and Technology of China, Institute of Fundamental and Frontier Sciences Dong, Huilong; Soochow University, Institute of functional Nano & Soft Materials Tretiak, Sergei; Los Alamos National Laboratory, T-1 group

Journal Name

ARTICLE TYPE

Cite this: DOI: 00.0000/xxxxxxxxxx

Recent Advances of Novel Ultrathin Two-Dimensional Silicon Carbides from a Theoretical Perspective

Liujiang Zhou,[a†*] Huilong Dong,[b†*] and Sergei Tretiak[c*]

Received Date
Accepted Date

DOI: 00.0000/xxxxxxxxxx

Compared to graphene with semimetallic features, two-dimensional (2D) silicon carbide (Si-C) materials constitute another highly promising family for opto-electronic applications owing the intrinsic electronic gaps. Recent theoretical studies of 2D Si-C materials thoroughly investigated their structure and properties. Herein, we overview these high-throughput approaches aiming to theoretically design 2D Si-C crystals. Graphene-like siligraphene and non-siligraphene are described in terms of morphology, physicochemical properties and potential applications based on the insights provided by simulations. In addition, the current progress of experimental exploration of 2D Si-C materials and underlying challenges are assessed as well.

1 Introduction

Two-dimensional (2D) materials, such as graphene and silicene, show very attractive physical and chemical properties, which are highly promising for the next generation of faster and smaller electronic devices.[1] However, the intrinsic semimetallicity significantly limits their applications to (opto)electronic devices frequently requiring tunable band-gap.[2] Consequently, numerous efforts have been devoted to open up the band gaps, including approaches such as substrate-induced gap,[3,4], fluorination[5] or hydrogenation,[6] application of an external gate,[7] fabrication of graphene nanoribbons,[8] doping,[9] etc. However, most of these findings have been proved to be difficult to attain in experiment. The feasibility challenges include well-controlled adsorption sites,[6] width of nanoribbons[8] and doping concentrations,[9] and thus altogether lead to high cost in experimental realization. Moreover, they usually produce either too small (tenths of eV)[3,4], or too large band gaps (>5 eV)[6] or chirality and width dependent gaps of nanoribbons.[2,8] Considering the compatibility in modern industry, the exploitation of 2D C- and/or Si-based crystals beyond graphene and silicene is a desirable direction which could greatly expand the family of 2D materials. 2D SiC in hexagonal phase is the most well-known representative of this materials class: it has an experimentally verified direct band gap of ∼3.72 eV[10] and has been extensively investigated theoretically. However, for optoelectronic applications such as the field effect transistors and photovoltaics, medium band gaps (i.e., 1.0−2.0 eV) are in a high demand. Moreover, intrinsic graphene and silicene sheets typically poorly suit for catalysis or gas sensing due to the absence of active sites. This altogether triggers further theoretical and experimental studies of 2D Si-C materials beyond the 1:1 elemental composition targeting wider applications. With different Si/C ratios and various geometries, the newly designed or predicted 2D Si-C materials could attain novel electronic, optical, mechanical, and chemical properties that go beyond those of graphene, silicene, and their allotropes.

The high-throughput simulations of materials using density functional theory (DFT) methods are matured and promising approaches to computationally investigate possible tunability of novel 2D crystals. The first principle DFT calculations frequently utilizing screened exchange hybrid density functionals Perdew, Burke, and Ernzerhof (PBE)[11] and by Heyd-Scuseria-Ernzerhof

[a] Institute of Fundamental and Frontier Sciences, University of Electronic Science and Technology of China, Chengdu 610054, P. R.China; E-mail: liujiang86@gmail.com.
[b] School of Chemistry and Materials Engineering, Changshu Institute of Technology, Changshu, Jiangsu 215500, P. R. China; E-mail:huilong_dong@126.com.
[b] Theoretical Physics and Chemistry of Materials, Los Alamos National Laboratory, Los Alamos, New Mexico 87545, United States; E-mail: serg@lanl.gov.
†Equally contributed to this work

(HSE06)[12,13] provide semi-quantitative accuracy for structural and electronic properties of these materials. The PBE functional usually underestimates the band gap while HSE06 level can be utilized to achieve more accurate band gap values. Furthermore, structural search and conformational optimizations include a variety of techniques such as (adaptive) genetic algorithms,[14,15] inverse design via multi-objective differential evolution,[16] Particle Swarm Optimization (PSO)[17], Cluster Expansion (CE) methods,[18] etc. Among them, PSO and CE methods have been used to explore 2D Si-C crystals. For example, by using PSO, Zhou *et al* reported a novel 2D Si-C material adopting the honeycomb lattice of pristine graphene (aka siligraphene), SiC_2.[2] Following this study, a series of 2D siligraphenes, SiC_3,[19] SiC_5,[20] SiC_7[21,22] proposed via mainly high-throughput DFT calculations, were systematically investigated in terms of geometry, electronic, optical, topological and magnetic properties, as well as their potential applications. Besides C-rich siligraphenes, their Si-rich counterparts, such as g-Si_nC for n = 3, 5 and 7 were reported as well using the PSO technique.[23] These studies brought out other low-dimensional systems and suggested enrichment of carbon chemistry. What is more, a recent discovery of non-siligraphene crystals exposed a new opportunity to seek novel Si and/or C-based 2D Si-C materials with structures beyond the hexagonal lattice. These new predicted non-siligraphene structures include planar tetracoordinated SiC_2 (pt-SiC_2),[24] penta-SiC_2,[25] SiC_6,[26] α-SiC_7,[22] SiC_8,[27] *t*-SiC,[28] *t*-Si_2C[28] and γ-silagraphyne,[28] etc. These theoretical findings disclosed extraordinary properties and new potential applications, thus triggering experimental exploration in this field towards desired functionalities.

In this mini-review, we focus on the modeling advances of the ultra-thin 2D Si-C crystals with a particular emphasis on the materials design approaches and the connections between morphology, physicochemical properties and potential applications. We outline a systematic categorization for various 2D Si-C materials according to structural motifs and then discuss their structural, mechanical, electronic, magnetic, optical properties as well as possible future applications. Lastly, we elaborate the current status and existing potential challenges in experiment and theory for 2D Si-C materials family and assess prospects of new opportunities for their future research and development. We further refer an interested reader to recent reviews oversewing development of materials design[29] and related 2D carbon-based materials including graphene/SiC heterostructure,[30] transition metal carbides,[31] B_2C,[32] etc.

2 Materials design approaches for 2D silicon carbide crystals

In recent years, the rapid development of 2D materials prediction was fueled by the high-throughput calculations.[14,15,17,18] Here, PSO and CE methods have been utilized to predict the 2D Si-C crystals. Due to the fact that Si and C have the preference of sp^3 and sp^2 hybridizations, respectively, the mix of Si and C atoms provide a versatile composition space to generate novel 2D Si-C crystals, including C-rich (flat) and Si-rich (low-buckled) siligraphene and non-siligraphene structures.

2.1 Particle Swarm Optimization

The PSO algorithm has been proven to be an efficient tool for the structural prediction of 2D crystals since the first realization of 2D B−C crystals in 2011.[33] The evolution of the structures in the PSO algorithm,[17,33,34] is inspired by the social behavior of flocking birds and is designed to solve problems related to a multidimensional optimization. Within this scheme, a structure in the search space is regarded as a particle. A set of particles is called a population or a generation. For 2D systems, all the structures are constrained in a plane. However, the atoms in layered materials may shift out of the plane, resulting in quasi-2D structures. To avoid the occurrence of instability of structure and to capture this feature of 2D materials, the atoms in the perpendicular direction within a certain range of $\pm\Delta z$ (e.g., $\Delta z \sim 0.1$ Å) are allowed to relax in the DFT optimizations, so that the 2D nature of the structure in question is retained. The PSO technique is instrumental for prediction of many siligraphene and non-siligraphene structures as exemplified in Figure 1a. Zhang et al. have verified the existence of a series of 2D Si-C siligraphenes using the PSO.[35] The obtained band gaps in these sheets vary from 0 to 2.5 eV based on PBE functional. It should be noted that all these stable monolayers possess a honeycomb lattice. Next, Fan et al. found a new type of 2D tetragonal inorganic material containing tetracoordiate silicons, named as t-SiC and t-Si_2C silagraphene, maintain both thermodynamic and mechanical stabilities predicted with the aid of the PSO.[28] More interestingly, six different silagraphyne sheets with higher pore sizes and the higher Poissons ratios are also determined. These silagraphyne sheets were suggested as potential candidates for separation membranes and catalytic materials.[28]

2.2 Cluster Expansion methods

First principles calculations combined with the CE approach[18] were used by Shi et al. to perform high-throughput calculations to explore the configuration space and describe the relationships between structure and properties, as well as limits of electronic tunability in 2D Si-C materials.[36] The CE method is established

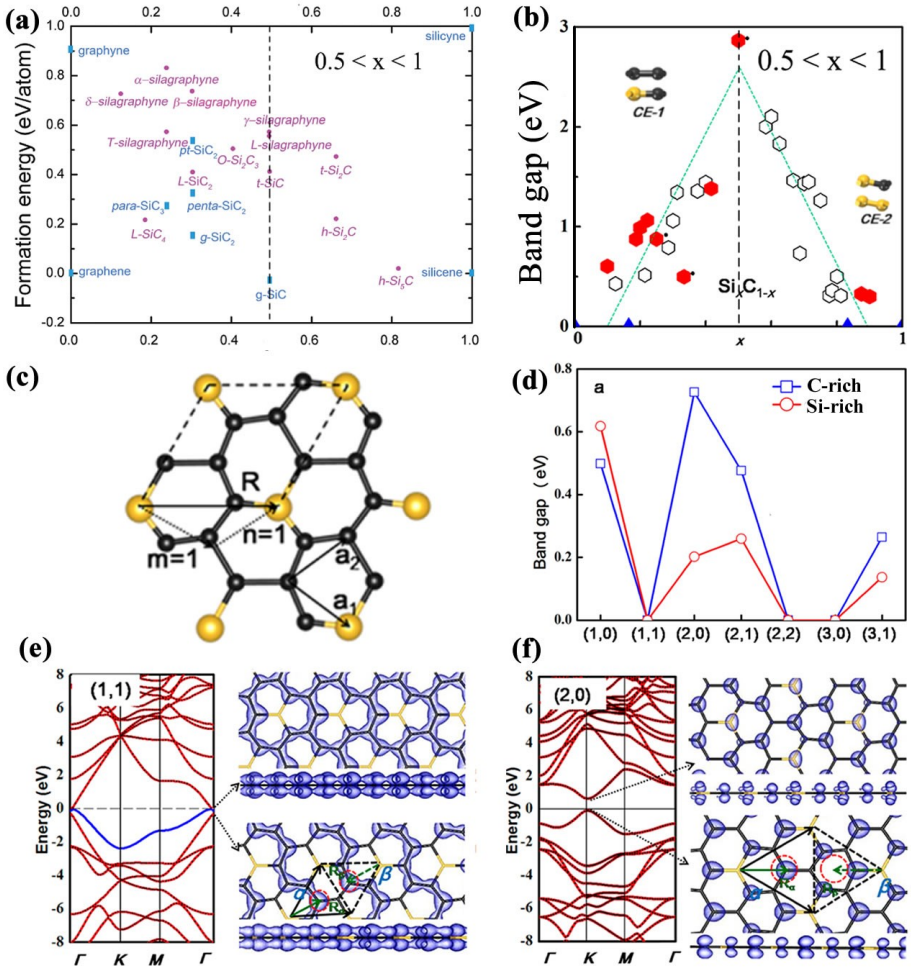

Fig. 1 (a) The calculated formation energies (E_f) of 2D Si_xC_{1-x} compounds with respect to elemental decomposition into graphene and silicene. When x = 0 (or x = 1), the calculated E_f for graphene (or silicene) are 0 eV/atom. Reproduced with permission from ref.[28] Copyright 2017 Royal Society of Chemistry. (b) Calculated band gaps of 2D Si_xC_{1-x} as the function of x based on PBE functional. Insets: The top and side views of the primitive cell adopted in CE-1 (planar) and CE-2 (buckling) calculations, respectively. Reproduced with permission from ref.[36] Copyright 2015 American Chemical Society. (c) The (1, 1) homogeneous structure characterized by the superlattice vector $\mathbf{R} = 1\mathbf{a}_1 + 1\mathbf{a}_2$. Reproduced with permission from ref.[36] Copyright 2015, American Chemical Society. (d) Band gaps of representative homogeneous Si_xC_{1-x} structures as a function of superlattice vector ranging from (1,0) to (3,1). Reproduced with permission from ref.[36] Copyright 2015, American Chemical Society. (e-f) Band structures of the (1,1), and (2,0) structures and the partial charge densities of the states near the Fermi level. The superatom models are illustrated in each plot of the charge density of valence band maximum (VBM). A vector dependence of the classification is identified by defining vectors R_α and R_β (green arrow in Figure 1e-f) connecting the vertex and the center (red dashed circle) of the superatoms α and β, respectively. Reproduced with permission from ref.[36] Copyright 2015, American Chemical Society.

in the theory of alloys, where the alloy Hamiltonian is mapped onto a generalized Ising Hamiltonian.[18] When applying to the predictions of 2D Si-C monolayer, the 2D system is considered as an alloy. Here the CE is defined by first assigning the occupation variables σ_i to each site i of the parent lattice: σ_i takes the value -1 or $+1$ due to the existing two atom types occupying the site, i.e., Si and C atoms. The CE calculations are divided into two parts: CE-1, from graphene to $Si_{0.5}C_{0.5}$, and CE-2, from $Si_{0.5}C_{0.5}$ to silicene. It is suggested that Si doping can effectively engineer the band gap of a graphene monolayer (Figure 1b) thus enabling optoelectronic device applications.

Importantly, Reference[36] reported existence of two distinct structural phases, homogeneous phase and in-plane hybrid phase with Si-C domains. The in-plane hybrid phase shows uniform semiconducting properties with widely tunable band gaps due to quantum confinement effect imposed by these domains. Nonethe-

less, either semiconducting or semimetallic traits can be achieved within homogeneous structures depending on a superlattice vector $\mathbf{R} = n\mathbf{a}_1 + m\mathbf{a}_2$ connecting two neighboring dopants Si or C, where $\mathbf{a}_1$ and $\mathbf{a}_2$ are the primitive lattice vectors of graphene, as illustrated in Figure 1c. Notably, all predicted siligraphenes with $(n - m) \bmod 3 = \pm 1$ possess sizable energy gaps ranging from 0.137 to 0.726 eV, while the rest with $(n - m) \bmod 3 = 0$ remain semimetallic (Figure 1d). This seems to be a universal rule similar to gap-chirality relationships in carbon nanotubes.[37]

The mechanism underpinning the structure-electron property relationships is clarified via analyzing the energy-resolved charge density and stems from the ionic potential difference between Si and C atoms (Figure 1e-f). Additionally, the origin of this rule is further explained by the superatom model proposed using group theory by Shima and Aoki.[38] In this model, the unit cell of the homogeneous sheet is considered as a supercell consisting of two superatoms, denoted as α and β (Figure 1e-f). The superatoms are further classified into type A_0 when there exists a hexagon in the center of each superatom and type A_C when an atom resides in such center (seeing the right panels of Figure 1e-f). Then the triangular lattices of the semimetallic sheets are constituted by two A_C superatoms, while that of a semiconducting sheets comprise the mixture of A_0 and A_C superatoms.[36]

3 2D Si-C materials: structures, electronic properties and potential applications

Due to the higher structural stability and attractive electronic and optical properties, the 2D Si-C sheets with a higher ratio of C/Si were studied frequently. It was found that both mechanical properties and anisotropy of 2D Si−C sheets are essentially associated with the presence and dispersion of Si atoms.[39] The Young's modulus and fracture stress generally decrease when the Si concentration increases from 0 to 0.2, and then slightly increase when Si concentration varies from 0.3 to 0.5.

Among the 2D Si−C crystals, the graphene-like siligraphenes have received special attentions due to their figures of merit making them particularly suitable for optoelectronics, energy storage and catalysis. Thus, we divided the scope of 2D Si−C materials into siligraphenes and non-siligraphenes. For siligraphenes, we further split them into two parts, C-rich (with a higher ratio of C atoms) and Si-rich (with a higher ratio of Si atoms) materials, according to the ratio of C/Si. Thus, we discuss next C-rich, Si-rich siligraphenes as well as non-siligraphenes in terms of structures, electronic properties and potential applications.

3.1 C-rich siligraphenes

The C-rich siligraphene (g-SiC_x) is formed by incorporating Si atoms into a honeycomb lattice of graphene. The g-SiC_x structures are strictly planar with hexagonal symmetry. The ratio of Si atoms in siligraphene ranges from 0 to 50%, and the hexagonal single-layer SiC (g-SiC) could be viewed as a special example of siligraphene. Isomorphous transformation has been demonstrated to be able to tune the electronic structures and even achieve the formation of Dirac cones (DCs) when g-SiC siligraphenes featuring C−C and Si−Si atom pairs.[40] This has been confirmed in the two isomorphous tetragonal phases, i.e., one with all C−C and Si−Si pairs aligning parallel to each other[40,41] and the other one with both pairs distributing more isotropically[40]) of g-SiC siligraphene. When we expand to other siligraphene with stoichiometry beyond the 1:1, despite there exists obvious similarity in structure, entirely different mechanical, electronic and optical properties could be exhibited compared to the parent graphene.

With respect to mechanical properties, the g-SiC_x sheets preserve rigorous isotropic Young's moduli and Poisson's ratios. In view of the robust mechanical performances, C-rich siligraphene family may facilitate the design of advanced 2D materials to meet demands for practical mechanical engineering applications.[42] Additionally, electronic properties of the g-SiC_x show great variability. The g-SiC_2, g-SiC_3, g-SiC_5, and g-SiC_7 have been extensively investigated in theory, with reported promising characteristics making them suitable for photovoltaic, electrocatalysis, energy storage, spintronics, and gas sensor technologies, which will be discussed next in detail.

3.1.1 g-SiC siligraphene

The g-SiC siligraphene possesses a planar geometry with a hexagonal space group of $P\bar{6}2m$ (Figure 2a). The optimized lattice parameter $a = 3.07$ Å and the Si−C bond length of 1.77−1.79 Åare predicted. Compared to graphene and silicene, the degeneracy of valence and conduction bands at K point is lifted out and a direct energy gap of 2.55 eV is opened (Figure 2b).[43,47] This is originated from the charge transfer from Si to C atoms and preferentiallocation of p^z orbital electrons on C atoms. Controlling the hydrogenation modes on g-SiC siligraphene is a promising approach to modulate the magnetic properties: a ferromagnetic semiconductor upon semi-hydrogenation over Si atoms and an antiferromagnetic semiconductor upon semi-hydrogenation over C atoms. Upon full hydrogenation, the chair-like and boat-like conformers are confirmed to be stable and are calculated to be nonmagnetic semiconductors with direct band gaps of 3.84 and 4.29 eV, respectively, both greatly larger than that of pristine g-SiC sheet (2.55 eV). Furthermore, new magnetic and electronic properties in g-SiC monolayer can be attained via the formation of substitutional impurities, vacancies and adatom decoration.[47]

Due to the reduced charge screening and the enhanced electronelectron correlation in the low-dimensional system, g-SiC is

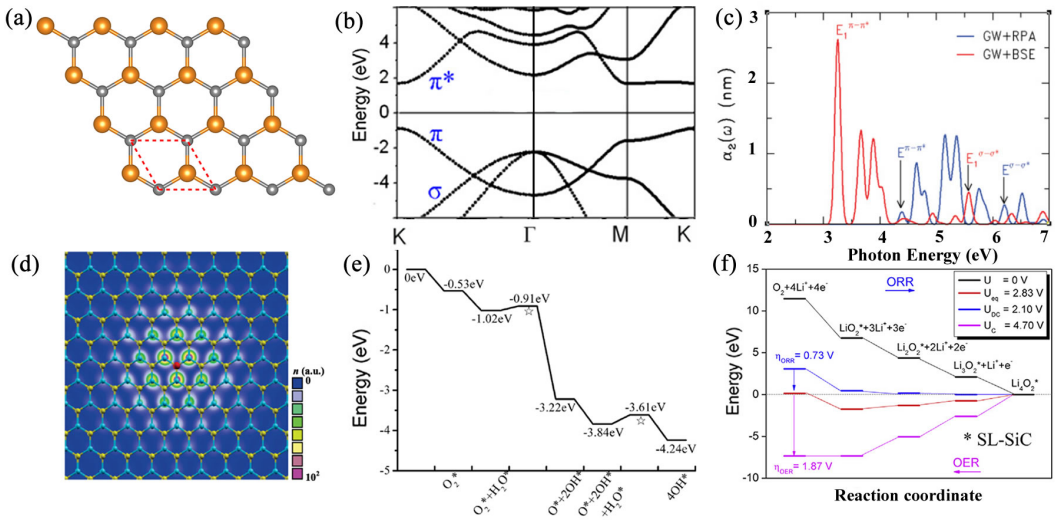

Fig. 2 (a) The crystalline structure of g-SiC, with red dash lines marking the unit cell. (b) The band structure of g-SiC calculated by PBE level. Reproduced with permission from ref.[43] Copyright 2011 Elsevier B.V. (c) Optical polarizability per unit area obtained from GW combined with random phase approximation (RPA) (blue) and BetheSalpeter equation (BSE) calculations. The theoretical spectra are broadened with a Gaussian smearing width of 0.15 eV. Reproduced with permission from ref.[44] Copyright 2011 American Physical Society. (d) The lowest bright exciton wave function of the SiC sheet. The hole is fixed at the top of a C atom (yellow sphere) and the electron amplitudes in arbitrary units are mainly distributed on Si atoms (cyan spheres) next to the hole. Reproduced with permission from ref.[44] Copyright 2011 American Physical Society. (e) Schematic energy profile for ORR elemental steps in alkaline media on g-SiC. Reproduced with permission from ref.[45] (f) The calculated free energy diagrams for ORR/OER catalyzed by g-SiC at zero potential (U = 0 V), equilibrium potential (U_{eq}), discharge potential (U_{DC}) and charge potential (U_C). Reproduced with permission from ref.[46] Copyright 2018 Elsevier B.V.

expected to exhibit a significant excitonic effect on the optical properties. Figure 2c presents the optical spectra obtained from Greens function and the screened Coulomb interaction (GW approximation) combining with the RPA or BSE calculations.[44] The onset energy of the GW corrected electron-hole continuum confirms the quasiparticle gap to be 4.42 eV, a large GW correction of 1.86 eV to the DFT band gap.[44] The lowest bright exciton wave function is located at about 3.25 eV rooting to the excitation between the π and the π^* states at the K point. This excition with the π character are mainly distributed on the nearest-neighbor Si atoms around the hole (Figure 2d),[44] indicating a localized exciton with a large exciton binding energy of 1.17 eV, strongly confining the quasiparticles.

The g-SiC siligraphene has been proposed as metal-free oxygen reduction reaction (ORR) electrocatalys to replace Pt-based catalysts due to its high concentrations of active reaction sites within a pure sheet. Zhang et al. reported that in an acidic environment, the g-SiC sheet exhibits a ORR catalytic activity comparable to Pt-based catalysts.[45] Importantly, g-SiC sheet possesses better catalytic activity in alkaline media when compared with Pt-based catalysts. As shown in Figure 2e, the ORR in Langmuir-Hinshelwood mechanism under an alkaline media is divided into two elemental steps: $O_2 + H_2O \rightarrow O + 2OH$ and $O + H_2O \rightarrow$ 2OH. These two steps have small activation energies being 0.11 and 0.23 eV, respectively. The second elemental step on g-SiC sheet is an exothermic process with a reaction energy of nearly 0.40 eV, while it is endothermic by 0.51 eV on the Pt(111) surface. Surprisingly, g-SiC catalyst does not have CO poisoning phenomenon that is a major obstacle in the conventional Pt-based catalysts. The above advantages suggest g-SiC siligraphene as a feasible metal-free ORR electrocatalyst in fuel cells.

Moreover, the electro-catalytic performance of g-SiC in the non-aqueous lithium-oxygen (Li-O_2) batteries has also been theoretically investigated.[46] The reaction steps of discharge process follow the sequence (a) $(Li^+ + e^-) + 2O^* \rightarrow LiO_2^*$, (b) $(Li^+ + e^-) + LiO_2^* \rightarrow Li_2O_2^*$, (c) $(Li^+ + e^-) + Li_2O_2^* \rightarrow Li_3O_2^*$, and (d) $(Li^+ + e^-) + Li_3O_2^* \rightarrow Li_4O_2^*$ (the * denotes the g-SiC_2 surface), with Li_2O acting as the discharge product. As depicted in Figure 2f, the free energy diagrams for ORR/OER catalyzed by g-SiC at different potentials illustrate that both the evaluated discharge (η_{ORR} = 0.73 V) and charge (η_{OER} = 1.87 V) overpotentials suitable to act as a cathode catalyst in non-aqueous Li$-O_2$ batteries.[46]

Besides these theoretical investigations of a single-layer structure, multilayer of g-SiC were also theoretically studited. Xu et al. found that the band structure varies dramatically from monolayer

to 3-layers, but remains essentially the same when going from 4 to 6-layers.[48] Unlike a monolayer, multilayer g-SiC exhibits indirect band gap. The indirect-to-direct band-gap transition indicates that a single-layer g-SiC is more suitable for optoelectronic applications. A further theoretical study revealed that for a bilayer g-SiC, the AB stacking wherein Si(C) atoms are positioned over C(Si) atoms is the most stable arrangement.[49] In addition, when multilayered g-SiC is examined for for catalysis applications, an increase of layer number merely changes the adsorption, activation and reaction energies of reaction intermediates, inferring the similar ORR catalytic activities.[45]

3.1.2 g-SiC_2 siligraphene

The graphene-like g-SiC_2 sheet is the first siligraphene structure theoretically predicted in 2013[2], which became the most well-studied siligraphene. The unit cell of g-SiC_2 exhibits a hexagonal space group of P$\bar{6}$2m with the optimized lattice parameter of $a = b \simeq 5.02$ Å. The structure of g-SiC_2 can be envisioned when two meta-positioned C atoms in graphene unit cell are replaced with Si atoms, as shown in Figure 3a. Thus, there are two types of C atoms: the C1 atoms connected directly with one C2 atom and two Si atoms, and C2 atoms bonded with three C1 atoms. Obviously, due to different bond lengths between Si-C and C−C bonds and electronegativity difference between Si and C atoms, these exists a small distortion of the hexagon. The degree of these distortions ultimately generates the variability in electronic structures. The DFT calculations indicate that g-SiC_2 is a direct band gap semiconductor with a gap of 1.09 eV (HSE06 level). Surprisingly, its derivative (n, 0), (n, n) nanotubes (with diameters greater than 8.0 Å) have almost the same gaps of 1.09 eV that are virtually independent on the chirality and diameter (Figure 3b). The direct band gap makes g-SiC_2 promising as a donor material in solar cells for light absorption, which has been further validated by theoretical simulations. As shown in Figure 3c, an excitonic solar cell constructed by using g-SiC_2 as a donor material and GaN monolayer as an acceptor material has a power conversion efficiency (PCE) limit of about 14.2%, confirming potential of use of g-SiC_2 in photovoltaics.[2]

Besides potential optical applications, the charge transfer processes within g-SiC_2 make it promising in electro-chemical catalysis. Based on charge analysis, the Si atoms are positively charged and can act as the Lewis acid site for adsorption of O_2 molecule.[50] The DFT simulations showed that O_2 prefers to be adsorbed on the two Si atoms in meta-position with bridge configuration, resulting in strong binding against O_2 (the absolute value of adsorption energy is 1.1 eV) and low barrier (0.25 eV) for dissociation of adsorbed O_2*. The g-SiC_2 exhibits a high rate-determining-step (RDS) activation barrier of 1.18 eV (the step of protonation of first OH*) in acid environment but a low RDS activation barrier of 0.16 eV (the step of formation of last two OH*) in alkaline environment. When considering the Eley-Rideal (ER) mechanism, g-SiC_2 shows a high overpotential of 0.96 V in acid environment but no overpotential in alkaline environment,[50] as illustrated in Figure 3d. Therefore, g-SiC_2 is suitable for metal-free ORR electrocatalyst in alkaline fuel cells.

Moreover, the electro-catalytic performance of g-SiC_2 in non-aqueous lithium-oxygen (Li-O_2) batteries has also been theoretically investigated.[46] The free energy diagrams for ORR/OER catalyzed by g-SiC_2 at different potentials as depicted in Figure 3e elucidate that both the evaluated discharge ($\eta_{ORR} = 0.85$ V) and charge ($\eta_{OER} = 2.20$ V) overpotentials are too large for a Li-O_2 battery. Theoretical analysis reveals that the high overpotentials are closely associated with the strong binding of O_2 to g-SiC_2.[46] Generally speaking, in contrast to its potential in H_2-O_2 fuel cells, g-SiC_2 is not ideal as cathode catalyst in non-aqueous Li−O_2 batteries.

Unlike its low performance in Li−O_2 batteries, g-SiC_2 is computationally predicted as a promising anchoring material for lithium-sulfur (Li−S) batteries. The binding strength of S_8 cluster and the soluble lithium polysulfide (Li_2S_n, including Li_2S_8, Li_2S_6, Li_2S_4, Li_2S_2 and Li_2S) species on g-SiC_2 was systematically investigated via DFT calculations.[52] Compared with other siligraphenes (g-SiC, g-SiC_3, and g-SiC_5), it is found that g-SiC_2 not only exhibits moderate binding strength with Li_2S_n, but also stabilizes the almost intact structural motifs and thus avoids its dissolution into the electrolyte. Thus g-SiC_2 shows the capability to immobilize the soluble Li_2S_n species by suppressing their shuttle effects. Moreover, the conductance of g-SiC_2 only marginally changes after adsorption of Li_2S_n species, enabling the redox reaction of the Li_2S_n species anchored on the surface via delivering free electrons.

Finally, there are also theoretical studies of g-SiC_2 as substrate for metal adsorption to design materials with adjustable magnetic properties that are applicable to spintronics. Recently, Golshan et al. reported the electronic and magnetic properties of 3d transition metals (TM) decorating g-SiC_2 by spin-polarized DFT calculations.[51] Upon different TM atoms with various concentrations adsorbed on SiC_2, various magnetic modes emerge (Figure 3f). The combination is a ferromagnetic half-metal (FMHM) for V adsorption at both low and high concentrations. As for Mn adsorption, the mixture displays FMHM and ferromagnetic metal (FMM) for Mn at low and high concentration, respectively. When Co is adsorbed on g-SiC_2, the complex behaves as a ferromagnetic bipolar system at low concentration, while for larger concentrations, it becomes an antiferromagnetic semiconductor. In contrast, the Ni-decorated g-SiC_2 always keeps non-magnetic semiconductor character. This points out a novel path to design materials with tunable magnetic orders from half-metallicity and bipolarity to

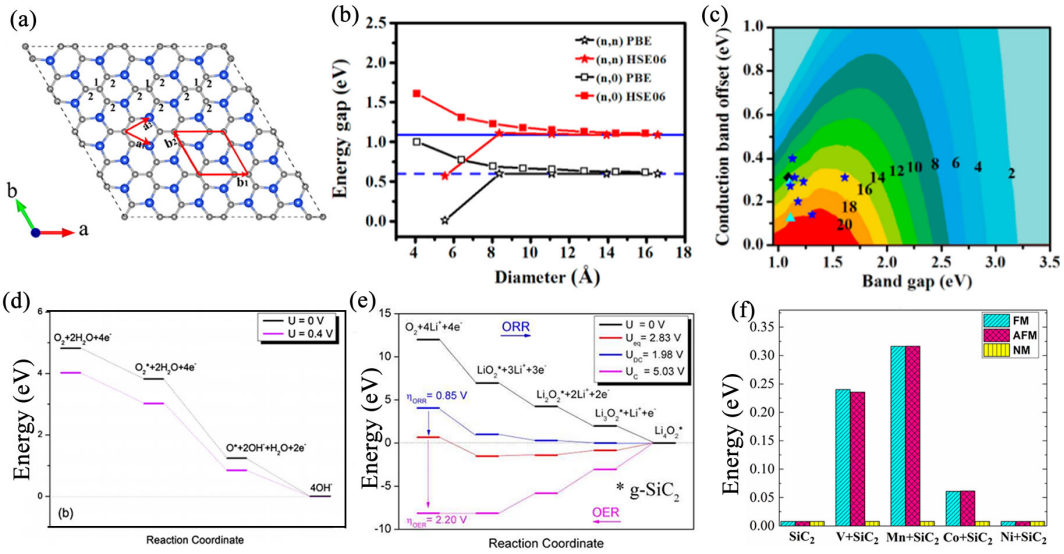

Fig. 3 Crystal structure of g-SiC_2 with unit cell marked as red lines. Red vectors $\mathbf{a}_1$, $\mathbf{a}_2$ are graphene lattice vectors; $\mathbf{b}_1$, $\mathbf{b}_2$ are g-SiC_2 lattice vectors. 1 and 2 denote the two crystallographic independent C atoms. Reproduced with permission from ref.[2] Copyright 2013 American Chemical Society. (b) Band gaps of (n, 0) ($3 \leq n \leq 10$) and (n, n) ($2 \leq n \leq 6$) g-SiC_2 tubes calculated by PBE and HSE06 levels. Reproduced with permission from ref.[2] Copyright 2013 American Chemical Society. Blue horizontal line: band gap of g-SiC_2 siligraphene. (c) The power conversion efficiency limits of the proposed g-SiC_2-based excitonic solar cells (XSC) as a function of the donor band gap and the conduction band offset. Reproduced with permission from ref.[2] Copyright 2013 American Chemical Society. (c) The entire catalytic cycle of g-SiC_2 as an electrocatalyst for ORR in alkaline environment. Reproduced with permission from ref.[50] Copyright 2015 Elsevier B.V. (d) The calculated free energy diagrams for ORR/oxygen evolution reaction (OER) catalyzed by g-SiC_2 at different potentials, $U = 0$ V, U_{eq}, U_{DC} and U_C. Reproduced with permission from ref.[46] Copyright 2018 Elsevier B.V. (e) Different magnetic-state energies of pristine g-SiC_2 and X+SiC_2 (X=V, Mn, Co or Ni) when g-SiC_2 is decorated by transition metal atoms in the most stable configurations for spintronic applications. Reproduced with permission from ref.[51] Copyright 2019 Elsevier B.V.

non-magnetic traits.

3.1.3 g-SiC_3 siligraphene

The atomic structure of g-SiC_3 siligraphene was first proposed by Zhao et al.[55]. Within g-SiC_3 siligraphene, a quarter of C atoms in para-position of the graphene honeycomb lattice are uniformly substituted by Si atoms, as shown in Figure 4a. The unit cell of g-SiC_3 exhibits the P6/mmm symmetry, with the optimized lattice parameter of $a = b \simeq 5.6$ Å. All the C atoms in g-SiC_3 are equal to each other and, as a result, all the bond angles in g-SiC_3 are perfectly 120° without any distortion, making it similar to the expanded graphene.[55]

The electronic analysis elucidates that g-SiC_3 is a semi-metal with a DC. Here the couplings among the ring composed by six C atoms (named as ring coupling mechanism) account for the formation of the DC feature, as unveiled in two isomorphous phases of g-SiC siligraphene.[56] Moreover, g-SiC_3 is illustrated to be a topological insulator (TI) with a non-trivial band gap of 0.43 meV, several orders of magnitude larger than that in graphene.[55] The electronic and electrical properties of g-SiC_3 are essentially unchanged under a compressive external strain of up to –9%,[57] indicating the high mechanical stability.

There is no evidence showing that g-SiC_3 has a potential to act as electro-catalyst. Due to the overbinding of O_2,[20] g-SiC_3 cannot effectively catalyze ORR as g-SiC_2 does. Another computational study revealed that there exists very high ORR and OER overpotentials when g-SiC_3 works as cathode catalysts in non-aqueous Li-O_2 batteries.[46] However, g-SiC_3 could be used for adsorption and catalytic decomposition of hydrazine (N_2H_4) under mild conditions.[19,58] The systematic DFT calculations revealed that N_2H_4 prefers to be chemically adsorbed on g-SiC_3 surface with anti configuration, and the N−N bond cleavage ($^*N_2H_4 \rightarrow 2^*NH_2$, * denotes the surface) appears as an initial step. By comparative studies, it is recommended that the pre-adsorbed NH_2 intermediates assisted by intermolecular decomposition should be the optimal pathway for catalytic decomposition of N_2H_4 on g-SiC_3, with N_2 and NH_3 being the products (Figure 4b). The highest activation barrier of 0.83 eV is obtained during the optimal pathway, indicating that g-SiC_3 may work as an efficient metal-free catalyst for catalytic decomposition of N_2H_4.[19]

Due to the metallic nature of g-SiC_3 and its activity against gas molecules, g-SiC_3 could be used for gas sensing. This is con-

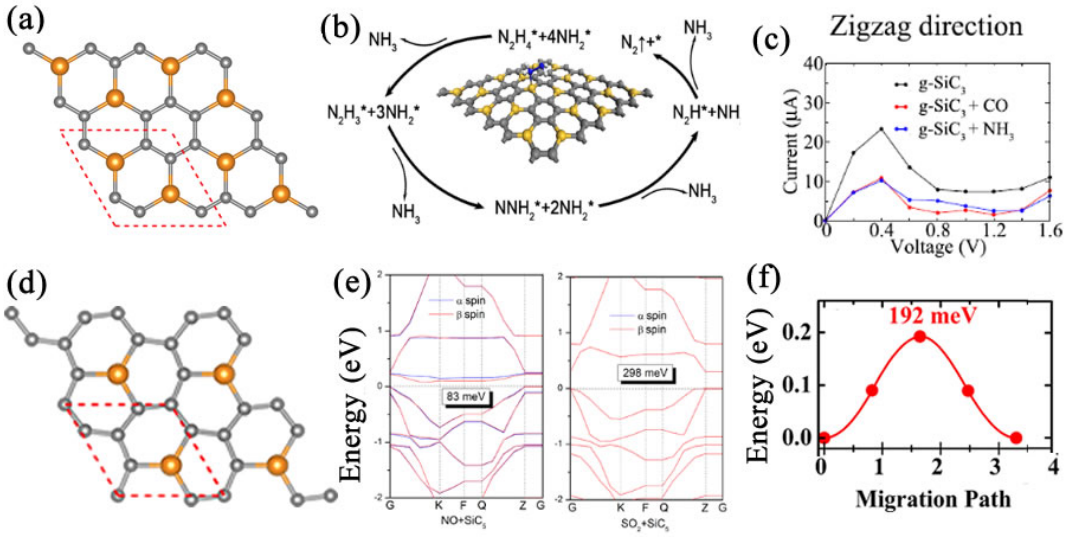

Fig. 4 (a) The crystalline structure of g-SiC_3, with red dash lines marking the unit cell. (b) Schematic depiction of the pathways of catalytic decomposition of hydrazine (N_2H_4) on g-SiC_3. Reproduced with permission from ref.[19] Copyright 2019 Elsevier B.V. (c) Current-voltage characteristics along the armchair and zigzag directions of the g-SiC_3 without and with adsorbed molecules when g-SiC_3 are applied for gas sensing of CO and NH_3. Reproduced with permission from ref.[53] Copyright 2019 American Chemical Society. (d) The crystalline structure of g-SiC_5 with the unit cell marked by red dash lines. (e) The theoretical band structures of NO and SO_2 adsorbed g-SiC_5 when used as gas sensor. The opened band gap values are marked. Reproduced with permission from ref.[20] Copyright 2017 Elsevier B.V. (f) The optimized Li-vacancy migration pathways on the up side of g-SiC_5 when used in Li-ion batteries (LIBs). Reproduced with permission from ref.[54] Copyright 2018 Elsevier B.V.

firmed by theoretically predicted adsorption behaviors and transport properties for CO and NH_3 molecules adsorbed on g-SiC_3 using first-principles calculations and the non-equilibrium Green's function method.[53] The physisorption of CO and NH_3 induces a small band gap in g-SiC_3. As a result, large resistivity variations are probed when CO and NH_3 molecules are adsorbed. Along the zigzag direction, adsorption of CO and NH_3 causes more obvious current decrease at a certain voltage (Figure 4c). The structural flexibility of the sensing medium and the susceptibility of Dirac states to symmetry-breaking distortions is proposed to explain the extraordinary sensitivity of g-SiC_3, which is expected to detect CO or NH_3 among diluted gases.

3.1.4 g-SiC_5 siligraphene

The g-SiC_5 was first predicted in 2015 as a ground state of $Si_{0.17}C_{0.83}$ material.[36] Within g-SiC_5, one C atom in the graphene honeycomb lattice is substituted by Si atom, as shown in Figure 4d. In the optimized structure of g-SiC_5, the unit cell exhibits $P\bar{6}$ symmetry, with a lattice parameter of $a = b \simeq 4.64$ Å.[20] There are two different C atoms in the unit cell: the C1 atoms connected directly with one Si atom and two other C atoms, and C2 atoms bonded with three C atoms. All the C1−Si−C1 and C1−C2−C1 angles are 120°. Band structure analysis of g-SiC_5 shows that it is semi-metallic with the conduction band minimum (CBM) and VBM contacting each other at the gamma point to form a DC.

The semimetallic nature of g-SiC_5 makes the sensing of gas molecules possible by measuring the change in conductance before and after adsorption. Computational investigations of the adsorption performance of 12 common gas molecules on g-SiC_5 reveal that the nucleophilic gas molecules exhibit stable chemisorption on g-SiC_5.[20] Among them, NO, HCHO and SO_2 show only moderate adsorption energies with g-SiC_5 in the range of 0.4-0.6 eV, and considerable band gaps (e.g., 83 meV for HCHO and 265 meV for SO_2) are opened in g-SiC_5 due to orbital hybridization, as shown in Figure 4e. The good selectivity and sensitivity make g-SiC_5 promising as the gas sensor for specific air pollutants like NO, HCHO and SO_2.[20]

In addition, the g-SiC_5 material has been proposed as an anode material for lithium-ion batteries (LIBs). The feasibility of g-SiC_5 and g-SiC_2 as high-capacity anode materials for LIBs was investigated with first-principles calculations.[54] Taking advantages from the high stability of graphene and the high capacity of silicene, the two siligraphenes show strong adsorption of Li atom, with the lowest values determined to be −2.536 eV and −2.567 eV for g-SiC_5 and g-SiC_2, respectively, at the corners of the hexagon far away from the Si atom. The g-SiC_5 and g-SiC_2 can be fully lithiated into Li_5SiC_5 and $Li_5Si_2C_4$, respectively, corresponding to the theoretical capacity of 1520 mAh/g and 1286 mAh/g. The dilute Li-vacancy migration pathways on up and down side sur-

faces of g-SiC_5 have diffusion barriers as low as 195 meV and 30 meV, respectively (see Figure 4f), both are lower than those of g-SiC_2. Therefore, g-SiC_5 is more favorable as an anode material for LIBs due to the higher theoretical capacity and lower diffusion barriers.

3.1.5 g-SiC_7 and and β-SiC_7 siligraphenes

The g-SiC_7 was confirmed as a low-energy structure in 2015 by using CE method.[36] The unit cell of g-SiC_7 belongs to the P6$\bar{m}$2 symmetry group, same as the hexagonal SiC monolayer, with the optimized lattice parameter of $a = b \simeq 5.3$ Å.[21] There is one Si atom and three different types of C atoms per unit cell, where the Si atom trigonally coordinates with the neighboring carbon atoms with C−Si−C bond angle of 120°, as shown in Figure 5a. The electronic analysis reveals that g-SiC_7 is a semiconductor with a direct band gap (E_g) of 0.76 eV (PBE level) or 1.13 eV (HSE06) (Figure 5b),[21] which is larger than that of the above-mentioned g-SiC_2 material. The band structure shows that both VBM and CBM are located at the K point (Figure 5b), showing potential of a light absorption. Based on the high fidelity G_0W_0 with BSE calculations, g-SiC_7 is shown to have an exciton binding energy of 0.55 eV. These simulations also placed the optical band gap at 1.0 eV being an ideal value for photovoltaics.[21] Compared to the g-SiC_2 and phosphorene,[60,61] g-SiC_7 possesses an enhanced light absorbance for the near infrared and visible region ranging from 0.7–3.0 eV, as depicted in Figure 5c.[21] Moreover, the absorbed photon flux (J_{abs}) of g-SiC_7 is 4.64 mA cm^{-2}, being larger than that in g-SiC_2 (4.06 mA cm^{-2}) and phosphorene (3.15 mA cm^{-2}),[62] which makes it usable as a donor material in excitonic solar cells. Moreover, the band gap of g-SiC_7 is tunable, with its value increasing when subject to biaxial strains from −10% to 10%.[21,63] Particularly, the band structure of g-SiC_7 changes from direct to indirect under 8% tensile strain and its electrical conductivity reaches the highest value when 6% tensile strain is applied.[63]

Considering the light weight of g-SiC_7, the hydrogen (H_2) storage characteristics of g-SiC_7 decorated with various light metals were explored.[59] Through DFT calculations, it is found that g-SiC_7 has strong binding with light metals like Li, Na, K, Mg, Ca, Sc, and Ti and thus exhibits the capability to counteract the competing metal clustering effect. The metal adatoms transfer a fraction of charges to g-SiC_7 monolayer, leaving partially charged metal center that could adsorb a maximum of 4 to 5 H_2 molecules. Moreover, the low concentration of metal doping could change the semiconducting g-SiC_7 into metallic material. The 12.5% is confirmed as the favorable doping concentration to reach a high H_2 gravimetric density for the metal decorated g-SiC_7. Particularly, the highest gravimetric density of 6.34 wt.% is achieved at the maximum Li concentration (16 H_2 on 4Li-SiC_7) with the ideal H_2 binding energies of 0.2–0.6 eV.[59]

The newly predicted β-SiC_7 siligraphene exhibits *P2mm* symmetry with lattice constants of $a = 5.27$ Å, $b = 4.57$ Å,[22] composing of hexagonal rings where the four Si atoms around carbon six ring are arranged as a rectangle (Figure 5d). The β-SiC_7 siligraphene exhibits a more stable stability compared to g-SiC_7. Calculations of electronic structures demonstrate that β-SiC_7 is a semiconductor with a direct band gap, where the VBM and CBM are located at the same k point along the path of Γ−X in the BZ. The obtained HSE06 band gap of β-SiC_7 is about 1.01 eV, referring a preferable efficiency of light absorption (Figure 5e). The calculated hole mobility of β-SiC_7 can reach ∼10 000 cm^2 V^{-1}s^{-1}. The proposed β-SiC_7/g-SiC_7 heterostructure can achieve a maximum PCE of 20.7%, indicating a potential of β-SiC_7 as a donor material for photovoltaics.[22]

3.2 Si-rich siligraphenes

Compared to the silicon carbides that have higher ratio of C than Si, the 2D Si_xC with higher concentration of Si atoms are much less studied due to the preferential sp^3 hybridization of Si atoms. Generally, the 2D Si_xC show buckled structures with relatively lower stability. Many of these structures are metallic or semimetallic. The potential applications of 2D Si_xC are also rarely reported.

Taking the Si-rich counterpart of siligraphenes, the structure and properties of graphitic g-Si_nC (n = 3, 5, 7) were theoretically investigated by Peng et al.[23] For g-Si_5C and g-Si_7C, the buckled structures were found to be slightly more stable than the corresponding planar structures. They share the same symmetry group with g-SiC_5 and g-SiC_7C but have larger lattice. As seen from the electronic bands of the buckled g-Si_5C (Figure 6a), it is semimetallic with a DC feature appearing around Γ point. Meanwhile, the buckled g-Si_7C is a semiconductor with an energy gap of 0.433 eV at the K point.

Particularly, the g-Si_3C is much more studied case than g-Si_5C and g-Si_7C materials due to its unique band structures as its C-rich counterpart g-SiC_3,[55,56] as shown in Figure 6b. Here the overlapping of p^z orbitals of C and Si atoms results in conjugated π orbitals extended throughout the framework, and thus produces the asymmetric distribution of wave functions around the C and Si atoms.[55] As a result, the g-Si_3C is semi-metallic with a DC featured band structure due to the ring coupling mechanism referring to the couplings of six Si ring atoms.[56]

The semi-metallic nature of g-Si_3C ensures its good electrical conductivity, based on which Dai et al. theoretically proposed and evaluated its potential as an anode material for LIBs.[64] It is reported that the adsorption energy for lithium atom on g-Si_3C (−2.58 eV) is large enough to ensure a good stability during the

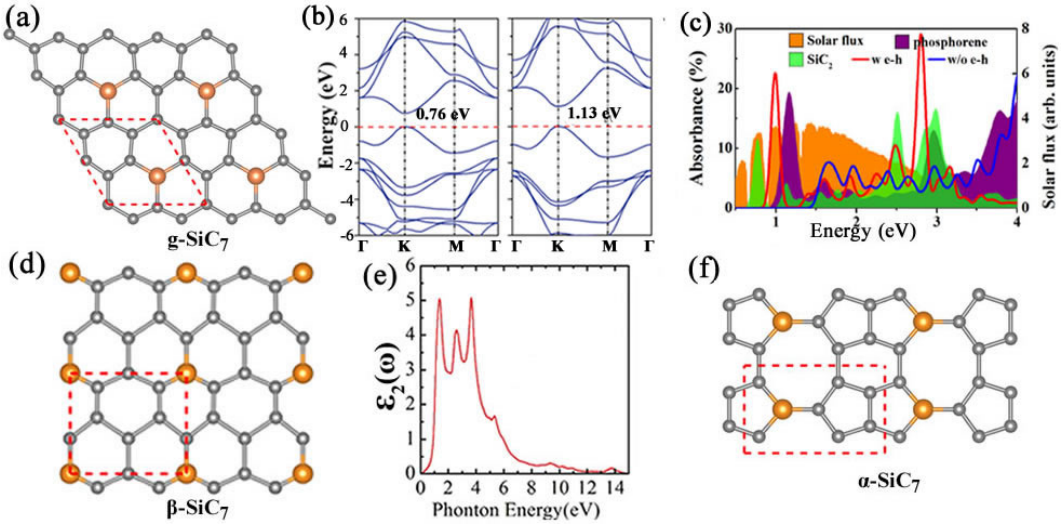

Fig. 5 (a) The crystalline structure of g-SiC_7, with red dash lines marked the unit cell. (b) Band structure of g-SiC_7 siligraphene obtained from PBE (left) and HSE06 (right) levels, respectively. Reproduced with permission from ref.[21] Copyright 2016 Royal Society of Chemistry. (c) The absorbance spectrum of g-SiC_7 (with and without electronhole interaction) overlapped to the incident AM1.5 G solar flux for the light donor material photovoltaic application, g-SiC_2 and phosphorene (along the armchair direction) are taken as comparison. Reproduced with permission from ref.[21] Copyright 2016 Royal Society of Chemistry. (d) Low-energy structure of β-SiC_7. (e) The imaginary part of the dielectric function of β-SiC_7 (HSE06 level). Reproduced with permission from ref.[22] Copyright 2019 Wiley-VCH. (f) Low-energy structure of α-SiC_7.

lithiation and de-lithiation processes. The fully lithiated g-Si_3C possesses a composition of $(Li_6Si_3C)_2$, corresponding to a high theoretical capacity of 1675 mAh/g and a low open-circuit voltage of 0.20 eV. However, the diffusion barrier of Li atom on g-Si_3C is 0.46 eV, which is relatively high and may hinder the practical applications of g-Si_3C in LIBs.

3.3 Non-siligraphene 2D Si-C structures

Though these siligraphenes were extensively studied with many reports, there are many more 2D SiC_x materials exhibiting structures that are quite different from the reference graphene honeycomb. Unlike the 3-coordinated Si atoms in siligraphenes that shows $sp^2 - sp^3$ hybridization characteristics, in many non-siligraphene cases, the Si atoms prefer sp^3 hybridization with a 4-coordination feature. It should be pointed out that all the 2D SiC_x structures discussed below have local minima in energy, with computationally validated structural, dynamic and thermodynamic stabilities.

3.3.1 t-SiC, t-Si_2C silagraphenes and γ-silagraphyne

In 2017 Fan et al. predicted two types of novel structural motifs with distinctive bonding patterns.[28] The first type of 2D Si-C sheets, containing t-SiC (Figure 7a) and t-Si_2C (Figure 7b) silagraphenes, can be characterized by tetragonal lattices. Among them, t-SiC monolayer is defined by each C atom bonding with four neighboring Si atoms in a puckered plane with a thickness of about 1 Å, constituting a quasi-planar four-coordinated rectangular moiety.[28] This moiety resembles our previously reported monolayers of ZrC,[65] TiN,[66] representing a lattice prototype in the family of 2D materials. Interestingly, this structure exhibits an insulator-semimetal transition when subject to the external strain,[28] indicating the promising applications for strain-dependent optoelectronic sensors. The t-Si_2C silagraphene forms an exactly flat rectangular structure, also adopting the four-coordinating way in the chemical bonding process. The optimized lattice constants are $a = 2.8$Å, $b = 9.1$ Å. Band structure calculations indicate that t-Si_2C is metallic. The $3p^z$ electrons of Si atoms and the $2p^z$ orbitals on the C atoms occupy the bands near Fermi level, which accounts for the metallic property in the t-Si_2C.[28] The second type of 2D Si-C sheet is named as γ-silagraphyne with acetylenic linkages ($-C\equiv C-$) and possesses high pore sizes and Poisson's ratio. These features make it a potential material for applications in separation membranes and catalysis. Moreover, γ-silagraphyne (Figure 7c) demonstrates a direct band gap of 0.89 eV, enabling a strong optical absorption in the visible-light region.[28]

3.3.2 pt-SiC_2 and penta-SiC_2 silagraphenes

As the earliest sample of 2D SiC_x structure, the planar tetra-coordinated SiC_2 (pt-SiC_2) silagraphene was predicted in 2011.[24] As shown in Figure 8a, the pt-SiC_2 silagraphene is purely planar with each Si atom bonding with four carbon atoms to form

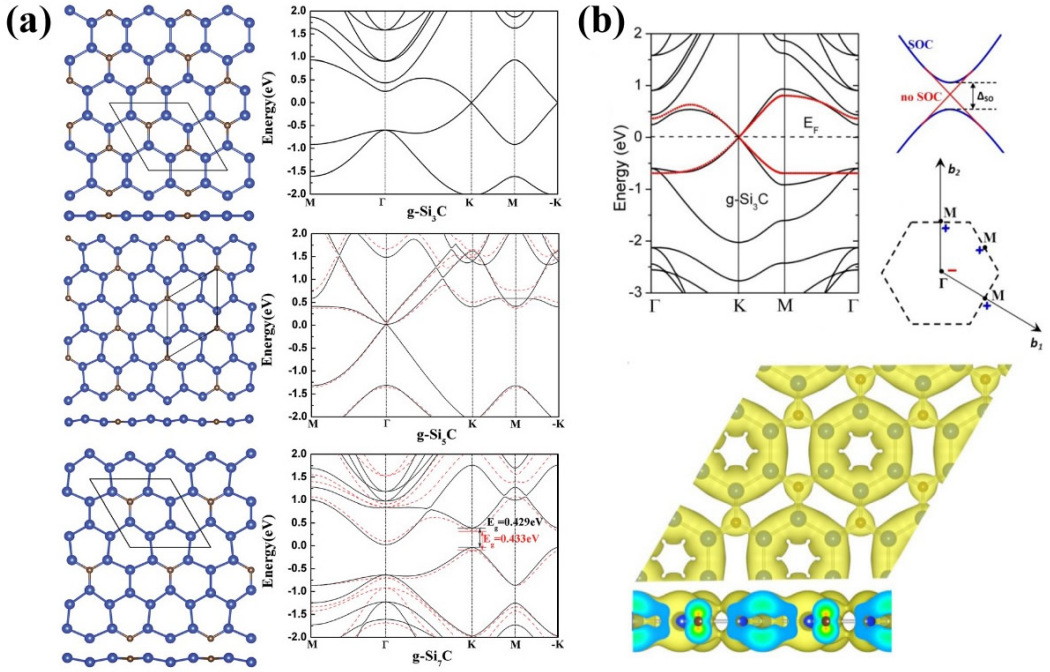

Fig. 6 (a) The atomistic structure (left), band structure (right) of g-Si_nC for n = 3, 5 and 7. In the right panel, the black solid and red dashed curves denote the band structure of the flat and buckled structures, respectively. Reproduced with permission from ref.[23] Copyright 2019 Royal Society of Chemistry. (b) Band structures of g-Si_3C along high-symmetry points (upper panel). Black and red lines represent the data obtained from DFT calculations and tight-binding model, respectively. Schematic representation of the enlarged view of the electronic bands with (blue) and without (red) spin-orbital coupling in the proximity of a Dirac point and Brillouin zone (BZ) path are also shown. Lower panel: The spatial distribution of the electron wave functions of the two Dirac bands in BZ. Both of top and side views are displayed. Reproduced with permission from ref.[55] Copyright 2014 American Physical Society.

a ptSi moiety, which is composed from the SiC_4 molecule as a building block. It is proposed that the planarity-preferred ethylene-like skeletons account for the planar SiC_2 network. The pt-SiC_2 is metallic with several energy levels crossing around the Fermi level. The metallic nature of SiC_2 mainly originates from the π-type C≡C bonds, which is significantly different from the semimetallic graphene or semiconducting g-SiC. To this end, there are no proposed applications or following studies on pt-SiC_2, however, more 2D materials with SiC_2 stoichiometry (including the g-SiC_2) are then inspired by the design of pt-SiC_2.

The penta-SiC_2 is another 2D Si-C material that shares the composition of SiC_2, which was theoretically designed by Lopez-Bezanilla and Littlewood in 2015.[25] The penta-SiC_2 is an isostructure of the penta-graphene,[68] where the two sp^3 hybridized C atoms are substituted by two Si atoms. All the pentagons in penta-SiC_2 are equal with four equivalent Si−C and one C−C edges, as shown in Figure 8b. Different from the g-SiC_2 or pt-SiC_2, penta-SiC_2 exhibits a significant buckled structure, with a thickness of 1.3 Å. The penta-SiC_2 is a semiconductor with an indirect band gap of 2.40 eV (HSE06 results).[67] A detailed analysis of the contribution of atomic orbitals revealed that the C p_z orbital dominates the CBM, while VBM is mainly composed from the p orbitals of C and Si atoms.[25] Compared with penta-graphene, a greater light absorption for both the visible and the ultraviolet spectral ranges is found for penta-SiC_2, making it suitable for photovoltaic applications. Moreover, penta-SiC_2 exhibits an enhanced electronic transport that originates from the delocalization of electronic states and smaller variations of the electrostatic potential within the system.[67] By applying in-plane tensile or compressible strain, the electronic transport properties could be effectively tuned by strain-engineering. Especially, under the uniaxial compressive strain of −8% along the a-direction, the hole mobility of penta-SiC_2 along the b-direction could be enhanced by almost three orders of magnitude up to 1.14×10^6 cm^2 V^{-1} s^{-1}. Therefore, p-SiC_2 may be also suitable for applications in electronic and optoelectronic devices.[69]

3.3.3 SiC_6 silagraphene

The 2D SiC_6 is composed of sp^2-hybridized C and sp^3-hybridized Si atoms with a *Cmma* symmetry.[26] As shown in Figure 8e, two

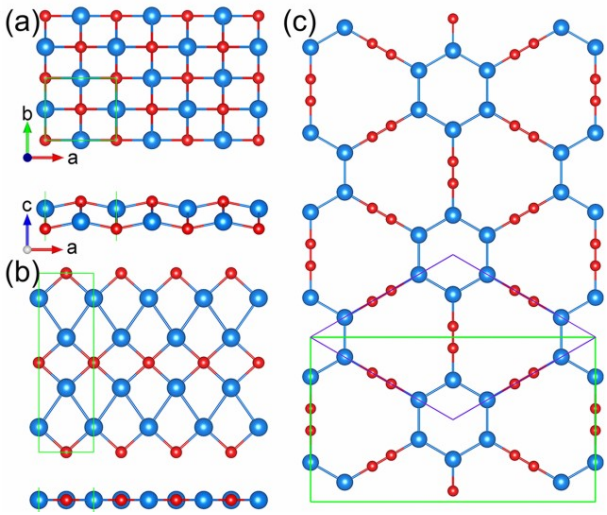

Fig. 7 Top (upper) and side (lower) views of the structure of (a) t-SiC, (b) t-Si_2C and (c) γ-silagraphyne monolayer. Blue balls: Si atoms; Red balls: C atoms. The rhombohedra (violet) and rectangular (green) unit cells are also indicated). Reproduced with permission from ref.[28] Copyright 2017, Royal Society of Chemistry.

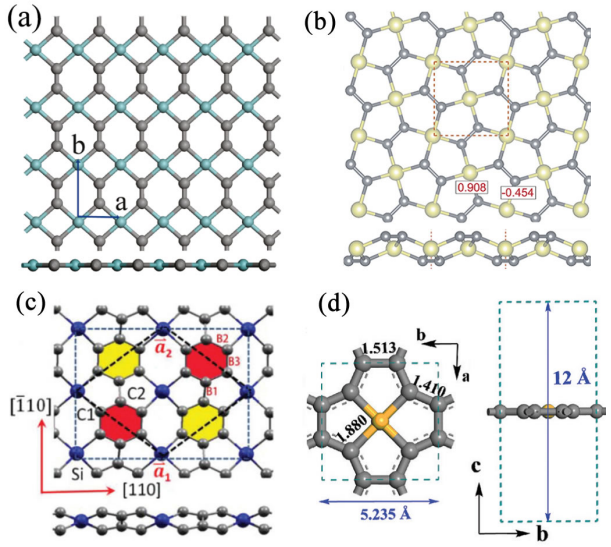

Fig. 8 The optimized geometric structures of (a) pt-SiC_2 (both top view and side view). Reproduced with permission from ref.[24] Copyright 2011 American Chemical Society. (b) penta-SiC_2 (both top view and side view). Reproduced with permission from ref.[67] Copyright 2016 Royal Society of Chemistry. (c) 2D SiC_6 (both top view and side view). Reproduced with permission from ref.[26] Copyright 2018, Royal Society of Chemistry. (d) 2D SiC_8 with indicated lattice parameters (both top view and side view). Reproduced with permission from ref.[27] Copyright 2018 Royal Society of Chemistry.

lattice basis vectors ($\mathbf{a}_1$) and ($\mathbf{a}_2$) are equal in length (6.5 Å) with an angle of 73.7°, forming a rhombic unit cell. The phenylsilane composed of a benzene ring and sp^3-hybridized Si atom are presumably the synthetic components of 2D SiC_6. The 2D SiC_6 has an indirect band gap of 0.225 eV (PBE) or 0.727 eV (HSE06). Under a compressive strain, SiC_6 could convert to a direct band gap semiconductor. While with the increase of tensile strain, the band gap firstly decreases to a minimum value and then increases. Subsequently, the hole and electron carrier mobilities in SiC_6 can be significantly improved by applying external strain. Moreover, SiC_6 is reported as an auxetic material with negative Poissons ratios, rendering its ability to bear a biaxial tensile strain up to 18%. Thus the 2D SiC_6 shows potentials for application in mechano-electronic devices.[26]

3.3.4 α-SiC_7 monolayer

The α-SiC_7 structure proposed in 2019 is one novel 2D structures with a composition of 1:7.[22] As shown in Figure 5f, the α-SiC_7 is composed of pentagons, hexagons, and heptagons in a flat basal plane, belonging to *P2mm* symmetry with optimized $a = 0.40$ nm, $b = 0.65$ nm. The α-SiC_7 material has better structural stability compared to that of the g-SiC_7. Calculations of electronic structures demonstrate that α-SiC_7 possesses the semimetallic feature with small electronic and hole pockets due to the existed bands crossing the Fermi energy.[22]

3.3.5 2D SiC_8 silagraphene

The planar SiC_8 silagraphene is initially constructed with the optimized stable $C_{12}H_8Si$ molecule as a building block. As shown in Figure 8d, the optimized 2D SiC_8 silagraphene exhibits *P4/mmm* symmetry and lattice parameters of $a = b \simeq 5.2$ Å.[27] In SiC_8, the Si atom adopts tetra-coordination with the surrounding C atoms, while the 8 C atoms form a conjugated eight-membered ring. The SiC_8 silagraphene is metallic, characterized by several energy bands near the Fermi level in the band structure. Its nature as a conductor and as an electron acceptor makes it possible to work as anode material in LIBs. The calculated theoretical capacity of SiC_8 sheet is 1297 $mAhg^{-1}$, much larger than that of graphene. Nonetheless, the diffusion of Li and Li^+ in SiC_8 silagraphene is acceptable due to low migration barriers, and the average cell voltages are close to the voltage value of the commercial anode materials.[27]

4 Experimental advances in synthesis of 2D silicon carbides

Reliable production of 2D atomically thin Si-C sheets with uniform size and properties is essential to translating superior properties into high-performance devices. Top-down (such as mechanical exfoliation)[70] and bottom-up (such as chemical vapor depo-

sition)[71,72] methods are the main routes for fabrication of 2D materials. Over about last decade, despite the numerous theoretical guidelines including structure predictions and simulations of electronic properties for 2D Si-C crystals, experimental fabrication techniques are still under-developed. In Si-C system, a stronger Si−C covalent bond length inhibits the overlaps of p−p orbital and thus leads to the preference of sp^3 hybridization of Si atoms across Si−C network,[73] which significantly differs from the pure sp^2 hybridization in graphene. This trend makes the interlayer coupling far stronger than the Van der Waals force in 2D Si-C monolayer and potentially disables its bare cleavage that requires extra post-etching process[74] thus entitling high fabrication cost. In particular, the fabricated Si-C system is a form of 3D bulk phase with a thickness in the scale of μm.[74] So that, synthetic routes toward the high-quality 2D Si-C crystals have to resort to other approaches.

In theory, Bijoy et al. reported that 2D layers of SiC can be exfoliated by lithiation with the average lithium intercalation potential of 0.2 V.[75] In experiment, to the best of our knowledge, only a few phases of 2D Si-C crystals have been prepared to be within the nanocale in experiment, that is, 2D SiC and SiC_2 siligraphenes. Lin et al. demonstrated that 2D SiC nanoflakes with thicknesses down to 0.5−1.5 nm could be possibly obtained via solution exfoliation by sonication of wurtzite SiC.[10] However, the reported *a*- and *c*-axis lattice constants of fabricated 2D SiC to be 0.266 and 0.694 nm, respectively, which are inconsistent with other experimental observations[76] and are very close to that of a typical graphite (0.246 and 0.67 nm). The use of exfoliation technique in producing 2D SiC from 3D SiC was also doubted by analyzing the lattice constant and X-ray powder diffraction peaks.[49] Yaghoubi and coworkers have thus speculated that what has been observed is a form of graphene.[49] Conversely, they also found different several-layer thick sheets of SiC siligraphene with different stacking orders as characterized by field-emission scanning electron micrographs and further analyzed by DFT calculations.[49] These experimental explorations constitute the synthetic progress toward high quality 2D Si-C sheets.

Following the top-down methods, the bottom-up approach was also reported for the quasi-2D SiC: the siligraphene with the thickness below 10 nm and lateral length of 0.3−5 μm was experimentally produced by reaction between graphene and a Si source.[77] Interestingly, the quasi-2D SiC_2 siligraphene was also found during this process as a byproduct with a thickness smaller than 2 nm, which can be stable for over 3 months in the ambient conditions. This technique resembles the formation of SiC nanotubes and nanowires via reaction of Si with C nanotubes.[76] Zou et al. reported a one-step solothermal route that can be utilized to prepare the 2H-SiC nanoflakes with the diameters of 200−500 nm and thickness of ∼15 nm.[78] Besides, β-SiC nanoplatelets were synthesized using waste plastic as the economical C source.[79] The final samples of nanoplatelets possess a hexagonal shape with the thicknesses of ∼50 nm, the lengths of 300−500 nm and the interplanar spacing of 0.25 nm. Next, the nanocrystalline, microcrystalline and epitaxial cubic SiC films were reported to be fabricated through the chemical vapor deposition method.[80] Chabi and co-workers synthesized the 2D SiC nanosheets with an average thickness of 2−3 nm and average size of 2 μm by merging the ultra-light 3D graphene foam and SiO at high temperature.[73]

In spite of these efforts, truly 2D siligraphene monolayer is yet to be realized due to mixed orbital hybridization modes (sp^2 and sp^3) present in 2D Si-C materials. Notably, the single-atom-thick SiC siligraphene nanograins assembling within the graphene oxide pores was observed by an atomic resolution scanning transmission electron microscopy.[81] Although the successful synthesis of Si-C monolayer is not claimed, the observation of small area nanograin may help to further refine experimental efforts towards realization of high quality 2D Si-C systems. Besides SiC and SiC_2 siligraphenes, Si-doped graphene could be considered as another siligraphene with a small ratio of Si/C. Zhang et al. reported that Si-doped graphene with a large surface area was synthesized using a chemical vapor deposition method at the doping levels of 2.7−4.5%.[82] However, the larger doping concentrations of Si atoms into graphene leading to larger band gaps are still challenging. We expect more reports on the experimental fabrication of single-atom-thick high quality monolayer or few-layer Si-C crystals will be emerging in the near future boosting the fundamental research and highlighting its practical applications.

5 Prospects and Summary

The fascinating physical and chemical properties render 2D Si-C crystals as promising materials for a variety of future technological uses. While great progress has been made to simulate properties and structure of 2D Si-C materials, so far, many theoretically predicted 2D Si-C systems are yet to be synthesized. The limited experimental observations of 2D Si-C still contain some contradicting signatures of known SiC nanosheets that need to be clarified. The lack of experimental synthetic routs is currently the largest bottleneck in the field, which hinders further exploration of these systems. We expect more 2D Si-C materials with high quality to be soon fabricated and measured towards realizing theoretically predicted functionalities that can be attained by the modern state-of-art preparation methods. Despite this setback, the modeling development of 2D Si-C materials is in a full swing due to their high potential for modern electronic industry. Besides, reducing dimensionality in structure, i.e., the exploration of 1D and 0D Si-C nanosystems also became a promising research direction somewhat making up for the deficiency of synthesis of pure 2D Si-C crystals. Here, numer-

ous cases have been investigated in theory and/or in experiment, including systems such as SiC nanoribborns,[83,84], nanowires,[76] nanotubes,[2,76,85–87] SiC-nanograins,[81] 0D quantum dots[88], and related heterostructures.[76] Besides 2D Si-C materials, theoretical design of 2D pure C-based materials, is another feasible way to advance the knowledge of carbon chemistry in modern device applications. Notably, multiple studies of 2D transition-metal carbides (such as TiC,[65] TaCX,[89] FeC_2,[90] etc.), III−C,[91] and IV−C[92] families are reported in experiment and/or theory. These studies could be further enriching the research direction for 2D C-based materials.

In summary, we have provided an overview on the recent progresses on theoretical modeling of 2D Si-C materials in terms of materials design, morphology, physicochemical properties, and indicated their potential applications. 2D Si-C crystals have an intriguing versatility of structures and properties. This makes 2D Si-C sheets to stand up in the burgeoning family of 2D layered materials with great promise for their applications in sensors, catalysts, electronics, spintronics, photovoltaics, etc. However, at the moment, experimental research seems to lag behind modeling advances. Subsequently, with the development of experimental fabrication routes, more fundamental and technological breakthroughs of high-quality of 2D Si-C crystals can be expected in the near future.

Conflicts of interest

There are no conflicts to declare.

Acknowledgements

L.Z. acknowledges the financial support from the University of Electronic Science and Technology of China. H.D. acknowledges the support of the National Natural Science Foundation of China (21703145). This work was performed in part at the Center for Integrated Nanotechnology (CINT), a U.S. Department of Energy and Office of Basic Energy Sciences user facility. S. T. acknowledges support from the Los Alamos National Laboratory (LANL) Directed Research and Development funds (LDRD). This research used resources provided by the LANL Institutional Computing Program.

Notes and references

1 X. Xu, C. Liu, Z. Sun, T. Cao, Z. Zhang, E. Wang, Z. Liu and K. Liu, *Chem. Soc. Rev.*, 2018, **47**, 3059–3099.

2 L.-J. Zhou, Y.-F. Zhang and L.-M. Wu, *Nano Lett.*, 2013, **13**, 5431–5436.

3 S. Y. Zhou, G.-H. Gweon, A. V. Fedorov, P. N. First, W. A. d. Heer, D.-H. Lee, F. Guinea, A. H. C. Neto and A. Lanzara, *Nature Mater.*, 2007, **6**, 770–775.

4 S. Y. Zhou, D. A. Siegel, A. V. Fedorov, F. E. Gabaly, A. K. Schmid, A. H. C. Neto, D.-H. Lee and A. Lanzara, *Nature Mater.*, 2008, **7**, 259–260.

5 H. ahin, M. Topsakal and S. Ciraci, *Phys. Rev. B*, 2011, **83**, 115432.

6 J. O. Sofo, A. S. Chaudhari and G. D. Barber, *Phys. Rev. B*, 2007, **75**, 153401.

7 H. Min, B. Sahu, S. K. Banerjee and A. H. MacDonald, *Phys. Rev. B*, 2007, **75**, 155115.

8 L. Yang, C.-H. Park, Y.-W. Son, M. L. Cohen and S. G. Louie, *Phys. Rev. Lett.*, 2007, **99**, 186801.

9 H. J. Xiang, B. Huang, Z. Y. Li, S.-H. Wei, J. L. Yang and X. G. Gong, *Phys. Rev. X*, 2012, **2**, 011003.

10 S. S. Lin, *J. Phys. Chem. C*, 2012, **116**, 3951–3955.

11 J. P. Perdew and A. Zunger, *Phys. Rev. B*, 1981, **23**, 5048–5079.

12 J. Heyd, G. E. Scuseria and M. Ernzerhof, *J. Chem. Phys.*, 2003, **118**, 8207–8215.

13 J. Heyd, G. E. Scuseria and M. Ernzerhof, *J. Chem. Phys.*, 2006, **124**, 219906.

14 S. Q. Wu, M. Ji, C. Z. Wang, M. C. Nguyen, X. Zhao, K. Umemoto, R. M. Wentzcovitch and K. M. Ho, *J. Phys.: Condens. Matter*, 2013, **26**, 035402.

15 C. W. Glass, A. R. Oganov and N. Hansen, *Comput. Phys. Commun.*, 2006, **175**, 713–720.

16 Y.-Y. Zhang, W. Gao, S. Chen, H. Xiang and X.-G. Gong, *Comput. Mater. Sci*, 2015, **98**, 51–55.

17 Y. Wang, J. Lv, L. Zhu and Y. Ma, *Phys. Rev. B*, 2010, **82**, 094116.

18 J. M. Sanchez, F. Ducastelle and D. Gratias, *Physica A*, 1984, **128**, 334–350.

19 F. Zheng, H. Dong, Y. Ji and Y. Li, *Appl. Surf. Sci.*, 2019, **469**, 316–324.

20 H. Dong, L. Wang, L. Zhou, T. Hou and Y. Li, *Carbon*, 2017, **113**, 114–121.

21 H. Dong, L. Zhou, T. Frauenheim, T. Hou, S.-T. Lee and Y. Li, *Nanoscale*, 2016, **8**, 6994–6999.

22 J. Guan, L. Zhang, K. Deng, Y. Du and E. Kan, *Adv. Theor. Simul.*, 2019, **2**, 1900058.

23 X. Tang, W. Liu, C. Luo, X. Peng and J. Zhong, *RSC Advances*, 2019, **9**, 12276–12281.

24 Y. Li, F. Li, Z. Zhou and Z. Chen, *J. Am. Chem. Soc.*, 2011, **133**, 900–908.

25 A. Lopez-Bezanilla and P. B. Littlewood, *J. Phys. Chem. C*, 2015, **119**, 19469–19474.

26 X. Liu, X. Shao, B. Yang and M. Zhao, *Nanoscale*, 2018, **10**, 2108–2114.

27 M.-J. Sun, X. Cao and Z. Cao, *Nanoscale*, 2018, **10**, 10450–

10458.
28 D. Fan, S. Lu, Y. Guo and X. Hu, *J. Mater. Chem. C*, 2017, **5**, 3561–3567.
29 R. Xu, X. Zou, B. Liu and H.-M. Cheng, *Mater. Today*, 2018, **21**, 391–418.
30 I. Shtepliuk, V. Khranovskyy and R. Yakimova, *Semicond. Sci. Technol.*, 2016, **31**, 113004.
31 X. Xiao, H. Wang, P. Urbankowski and Y. Gogotsi, *Chem. Soc. Rev.*, 2018, **47**, 8744–8765.
32 Q. Tang, Z. Zhou and Z. Chen, *Wiley Interdiscip. Rev.: Comput. Mol. Sci.*, 2015, **5**, 360–379.
33 X. Luo, J. Yang, H. Liu, X. Wu, Y. Wang, Y. Ma, S.-H. Wei, X. Gong and H. Xiang, *J. Am. Chem. Soc.*, 2011, **133**, 16285–16290.
34 Y. Wang, J. Lv, L. Zhu and Y. Ma, *Comput. Phys. Commun.*, 2012, **183**, 2063–2070.
35 J. Zhang, J. Ren, H. Fu, Z. Ding, H. Li and S. Meng, *Sci. China Phys. Mech. Astron.*, 2015, **58**, 106801.
36 Z. Shi, Z. Zhang, A. Kutana and B. I. Yakobson, *ACS Nano*, 2015, **9**, 9802–9809.
37 R. Saito, M. Fujita, G. Dresselhaus and M. S. Dresselhaus, *Phys. Rev. B*, 1992, **46**, 1804–1811.
38 N. Shima and H. Aoki, *Phys. Rev. Lett.*, 1993, **71**, 4389–4392.
39 D.-T. Nguyen and M.-Q. Le, *Superlattices Microstruct.*, 2016, **98**, 102–115.
40 X. Qin, Y. Liu, X. Li, J. Xu, B. Chi, D. Zhai and X. Zhao, *J. Phys. Chem. Lett.*, 2015, **6**, 1333–1339.
41 L. Wang and H. Sun, *J. Mol. Model.*, 2012, **18**, 4811–4818.
42 X. K. Lu, T. Y. Xin, Q. Zhang, Q. Xu, T. H. Wei and Y. X. Wang, *Nanotechnology*, 2018, **29**, 315701.
43 L. Pan, H. J. Liu, Y. W. Wen, X. J. Tan, H. Y. Lv, J. Shi and X. F. Tang, *Physics Letters A*, 2011, **375**, 614–619.
44 H. C. Hsueh, G. Y. Guo and S. G. Louie, *Phys. Rev. B*, 2011, **84**, 085404.
45 P. Zhang, B. B. Xiao, X. L. Hou, Y. F. Zhu and Q. Jiang, *Sci Rep*, 2014, **4**, 1–8.
46 H. Dong, Y. Ji, T. Hou and Y. Li, *Carbon*, 2018, **126**, 580–587.
47 E. Bekaroglu, M. Topsakal, S. Cahangirov and S. Ciraci, *Phys. Rev. B*, 2010, **81**, 075433.
48 X. Lin, S. Lin, Y. Xu, A. A. Hakro, T. Hasan, B. Zhang, B. Yu, J. Luo, E. Li and H. Chen, *J. Mater. Chem. C*, 2013, **1**, 2131–2135.
49 A. Yaghoubi, K. Masenelli-Varlot, O. Boisron, S. Ramesh and P. Melinon, *Chem. Mater.*, 2018, **30**, 7234–7244.
50 H. Dong, B. Lin, K. Gilmore, T. Hou, S.-T. Lee and Y. Li, *J. Power Sources*, 2015, **299**, 371–379.
51 M. F. Saadi, R. Safaiee and M. M. Golshan, *Appl. Surf. Sci.*, 2019, **481**, 484–497.
52 Y. Zhao, J. Zhao and Q. Cai, *Appl. Surf. Sci.*, 2018, **440**, 889–896.
53 V. Babar, S. Sharma and U. Schwingenschlögl, *J. Phys. Chem. C*, 2019, **123**, 13104–13109.
54 H. Wang, M. Wu, X. Lei, Z. Tian, B. Xu, K. Huang and C. Ouyang, *Nano Energy*, 2018, **49**, 67–76.
55 M. Zhao and R. Zhang, *Phys. Rev. B*, 2014, **89**, 195427.
56 X. Qin, Y. Wu, Y. Liu, B. Chi, X. Li, Y. Wang and X. Zhao, *Sci. Rep.*, 2017, **7**, 10546.
57 M. Houmad, M. H. Mohammed, R. Masrour, A. El Kenz and A. Benyoussef, *J. Phys. Chem. Solids*, 2019, **127**, 231–237.
58 F. Zheng, H. Dong, Y. Ji and Y. Li, *Int. J. Hydrog. Energy*, 2019, **44**, 6055–6064.
59 S. R. Naqvi, T. Hussain, W. Luo and R. Ahuja, *Nano Res.*, 2018, **11**, 3802–3813.
60 L. Kou, C. Chen and S. C. Smith, *J. Phys. Chem. Lett.*, 2015, **6**, 2794–2805.
61 H. Liu, A. T. Neal, Z. Zhu, Z. Luo, X. Xu, D. Tománek and P. D. Ye, *ACS Nano*, 2014, **8**, 4033–4041.
62 L. Zhou, J. Zhang, Z. Zhuo, L. Kou, W. Ma, B. Shao, A. Du, S. Meng and T. Frauenheim, *J. Phys. Chem. Lett.*, 2016, **7**, 1880–1887.
63 M. Houmad, I. Essaoudi, A. Ainane, A. El Kenz, A. Benyoussef and R. Ahuja, *Optik*, 2019, **177**, 118–122.
64 Y. Dong, W. Wei, X. Lv, B. Huang and Y. Dai, *Appl. Surf. Sci.*, 2019, **479**, 519–524.
65 L. Zhou, B. Shao, W. Shi, Y. Sun, C. Felser, B. Yan and T. Frauenheim, *2D Mater.*, 2016, **3**, 035022.
66 L. Zhou, Z. Zhuo, L. Kou, A. Du and S. Tretiak, *Nano Lett.*, 2017, **17**, 4466–4472.
67 G. R. Berdiyorov and M. El-Amine Madjet, *RSC Advances*, 2016, **6**, 50867–50873.
68 S. Zhang, J. Zhou, Q. Wang, X. Chen, Y. Kawazoe and P. Jena, *Proc. Natl. Acad. Sci. U.S.A.*, 2015, **112**, 2372–2377.
69 Y. Xu, Z. Ning, H. Zhang, G. Ni, H. Shao, B. Peng, X. Zhang, X. He, Y. Zhu and H. Zhu, *RSC Adv.*, 2017, **7**, 45705–45713.
70 K. Lee, H.-Y. Kim, M. Lotya, J. N. Coleman, G.-T. Kim and G. S. Duesberg, *Adv. Mater.*, 2011, **23**, 4178–4182.
71 X. Li, W. Cai, J. An, S. Kim, J. Nah, D. Yang, R. Piner, A. Velamakanni, I. Jung, E. Tutuc, S. K. Banerjee, L. Colombo and R. S. Ruoff, *Science*, 2009, **324**, 1312–1314.
72 Y.-H. Lee, X.-Q. Zhang, W. Zhang, M.-T. Chang, C.-T. Lin, K.-D. Chang, Y.-C. Yu, J. T.-W. Wang, C.-S. Chang, L.-J. Li and T.-W. Lin, *Adv. Mater.*, 2012, **24**, 2320–2325.
73 S. Chabi, H. Chang, Y. Xia and Y. Zhu, *Nanotechnology*, 2016, **27**, 075602.

74 M. Syväjärvi, R. Yakimova and E. Janzén, *J. Cryst. Growth*, 2000, **208**, 409–415.

75 T. K. Bijoy, J. Karthikeyan and P. Murugan, *J. Phys. Chem. C*, 2017, **121**, 15106–15113.

76 X.-H. Sun, C.-P. Li, W.-K. Wong, N.-B. Wong, C.-S. Lee, S.-T. Lee and B.-K. Teo, *J. Am. Chem. Soc.*, 2002, **124**, 14464–14471.

77 S. Lin, S. Zhang, X. Li, W. Xu, X. Pi, X. Liu, F. Wang, H. Wu and H. Chen, *J. Phys. Chem. C*, 2015, **119**, 19772–19779.

78 G. Zou, C. Dong, K. Xiong, H. Li, C. Jiang and Y. Qian, *Appl. Phys. Lett.*, 2006, **88**, 071913.

79 Z. Ju, L. Xu, Q. Pang, Z. Xing, X. Ma and Y. Qian, *Nanotechnology*, 2009, **20**, 355604.

80 H. Zhuang, N. Yang, L. Zhang, R. Fuchs and X. Jiang, *ACS Appl. Mater. Interfaces*, 2015, **7**, 10886–10895.

81 T. Susi, V. Skákalová, A. Mittelberger, P. Kotrusz, M. Hulman, T. J. Pennycook, C. Mangler, J. Kotakoski and J. C. Meyer, *Sci. Rep.*, 2017, **7**, 4399.

82 S. J. Zhang, S. S. Lin, X. Q. Li, X. Y. Liu, H. A. Wu, W. L. Xu, P. Wang, Z. Q. Wu, H. K. Zhong and Z. J. Xu, *Nanoscale*, 2016, **8**, 226–232.

83 J. Cui, Z. Zhang, D. Liu, D. Zhang, W. Hu, L. Zou, Y. Lu, C. Zhang, H. Lu, C. Tang, N. Jiang, I. P. Parkin and D. Guo, *Nano Lett.*, 2019, **19**, 6569–6576.

84 X. Zheng, X. Chen, L. Zhang, L. Xiao, S. Jia, Z. Zeng and H. Guo, *2D Mater.*, 2017, **4**, 025013.

85 G. Mpourmpakis, G. E. Froudakis, G. P. Lithoxoos and J. Samios, *Nano Lett.*, 2006, **6**, 1581–1583.

86 W. Shi, S. Wu and Z. Wang, *Physica E*, 2016, **81**, 192–195.

87 M. Menon, E. Richter, A. Mavrandonakis, G. Froudakis and A. N. Andriotis, *Phys. Rev. B*, 2004, **69**, 115322.

88 D. Dai, X. Guo and J. Fan, *Appl. Phys. Lett.*, 2015, **106**, 053115.

89 L. Zhou, W. Shi, Y. Sun, B. Shao, C. Felser, B. Yan and T. Frauenheim, *2D Mater.*, 2016, **3**, 035018.

90 T. Zhao, J. Zhou, Q. Wang, Y. Kawazoe and P. Jena, *ACS Appl. Mater. Interfaces*, 2016, **8**, 26207–26212.

91 Y. Xu, J. Dai and X. C. Zeng, *J. Phys. Chem. Lett.*, 2016, **7**, 302–307.

92 T.-Y. Lü, X.-X. Liao, H.-Q. Wang and J.-C. Zheng, *J. Mater. Chem.*, 2012, **22**, 10062–10068.